

High-fidelity robotic PCR amplification

Vincent Beguin^{1,*}, Jean Grétillat^{2,*}, Kornelija Kaminskaitė³, Simona Juzenas³, Dainius Kirsnauskas³, Pierre-Yves Burgi⁴, Samuel Wenger¹, Valentin Remonnay¹, Silvia Angeloni¹, Patrick Neuenschwander¹, Bart van der Schoot⁵, Augustin Cerveaux⁵, Thomas Heinis⁶, Renaldas Raisutis⁷, Martin Jost⁸, Lukas Zemaitis³, Ignas Galminas^{3#}, Jérôme Charmet^{1,2,9#}

1. *School of Engineering-HE-Arc Ingénierie, HES-SO University of Applied Sciences Western Switzerland, Neuchâtel, Switzerland*
2. *School of Precision and Biomedical Engineering, University of Bern, Bern, Switzerland*
3. *Department of DNA data storage, Genomika, Kaunas, Lithuania*
4. *IT Department, University of Geneva, Geneva, Switzerland*
5. *Seyonic SA, Neuchâtel, Switzerland*
6. *Department of Computing, Imperial College London, London, United Kingdom*
7. *Ultrasound Research Institute, Kaunas University of Technology, Kaunas, Lithuania*
8. *MABEAL GmbH, Graz, Austria*
9. *Warwick Medical School, University of Warwick, Coventry, United Kingdom*

* the authors contributed equally to the work.

Abstract

Polymerase chain reaction (PCR) underpins modern molecular biology, yet its deployment in emerging domains such as DNA data storage and distributed diagnostics remains constrained by bulky thermocyclers, complex thermal hardware, and contamination-prone workflows. Here, we present an autonomous robotic PCR platform that redefines thermocycling as a motion-controlled process rather than a temperature-controlled device. The system employs a programmable robotic liquid handler to execute PCR entirely within sealed pipette tips, repeatedly immersing and withdrawing reaction volumes in a single temperature-stabilized oil bath to realize denaturation, annealing, and extension steps through precise spatiotemporal control. This architecture eliminates conventional thermocyclers and enables fully enclosed reactions with complete sample recovery. We demonstrate that the robotic system achieves amplification efficiency and sequencing fidelity comparable to high-performance commercial thermocyclers when applied to DNA-encoded datasets. Beyond performance parity, the platform minimizes reagent consumption, suppresses cross-contamination through physical isolation, and supports parallelization through robotic scheduling rather than hardware duplication. By abstracting PCR thermocycling into a robotically orchestrated manipulation task, this work establishes a generalizable framework for automated biochemical processing and positions robotic control as a central design axis for scalable, low-cost molecular workflows.

Keywords: robotic PCR, contamination control, laboratory automation, DNA data storage

Introduction

The exponential growth of digital data has created an urgent need for sustainable, long-term storage solutions¹. DNA has emerged as a compelling alternative, offering theoretical storage densities exceeding 1 exabyte per cubic millimeter and stability spanning millennia under appropriate conditions^{2,3}. Unlike conventional storage media that degrade within decades, DNA's inherent molecular stability and information density make it uniquely suited for archival applications requiring century-scale data preservation^{4,5}.

Despite significant advances in DNA data storage technology, the transition from laboratory demonstrations to practical archival systems remains constrained by workflow complexity. The complete pipeline—encompassing synthesis, storage, retrieval, amplification, library preparation, and sequencing—requires multiple specialized instruments and protocols^{6–8}. Widespread adoption by archival institutions demands integration of these steps into autonomous, end-to-end platforms requiring minimal human intervention.

Amplification is a critical step in this workflow, essential for both data retrieval and re-amplification of archived samples^{9,10}. However, unlike diagnostic or research applications where speed is prioritized, DNA data storage workflows demand reliability, contamination control, and long-term operational sustainability over throughput. These requirements create an opportunity to fundamentally rethink amplification strategies for autonomous operation and robotic integration.

To develop an automation-compatible amplification approach, we revisited PCR's evolution to identify design principles suited for robotic implementation. The original PCR protocol developed by Kary Mullis employed manual sample transfers between three temperature-controlled water baths—a simple yet effective technique that achieved rapid thermal transitions through direct sample-to-bath contact^{11,12}. Subsequent automated thermocyclers transformed PCR accessibility, with current high-performance instruments achieving heating rates approaching 5 °C/s through sophisticated thermal control systems^{13,14}. However, these devices function as standalone units that resist integration into robotic workflows, requiring separate handling steps and redundant equipment that compound system complexity.

Microfluidic platforms emerged as an alternative, leveraging enhanced heat transfer from increased surface-to-volume ratios to enable integrated sample processing^{15–17}. Digital PCR (dPCR) extended this paradigm by partitioning reactions for absolute quantification with improved sensitivity^{18,19}. Despite these advances, microfluidic approaches are difficult to integrate with DNA data storage workflows, primarily because complete sample retrieval from microfluidic devices—essential for downstream sequencing—is challenging²⁰. Furthermore, their limited flexibility impedes adaptation to evolving protocols, as modifications typically necessitate new chip designs rather than simple software updates^{21,22}.

Current automation-compatible solutions partially address these bottlenecks but introduce redundant instrumentation. Commercial robotic liquid-handling platforms, such as Opentrons, offer programmable automation yet require multiple liquid transfers between pipette tips, PCR tubes, or plates, followed by amplification in separate thermocyclers^{23,24}. This multi-step workflow demands both robotic handlers and dedicated thermocyclers, while introducing contamination risks and mechanical complexity through repeated transfers and lid manipulations²⁵.

Here, we introduce a disruptive approach that revisits the original water bath-based PCR method and integrates it with modern robotic liquid-handling technology, eliminating equipment redundancy. Our platform, termed PCRobot, employs a robotic unit with an integrated pipettor to perform amplification

via controlled immersion and withdrawal of sample-loaded tips in a single heated oil bath. This configuration achieves heating rates comparable to advanced thermocyclers ($\sim 5\text{ }^{\circ}\text{C/s}$) while exploiting passive air convection for cooling.

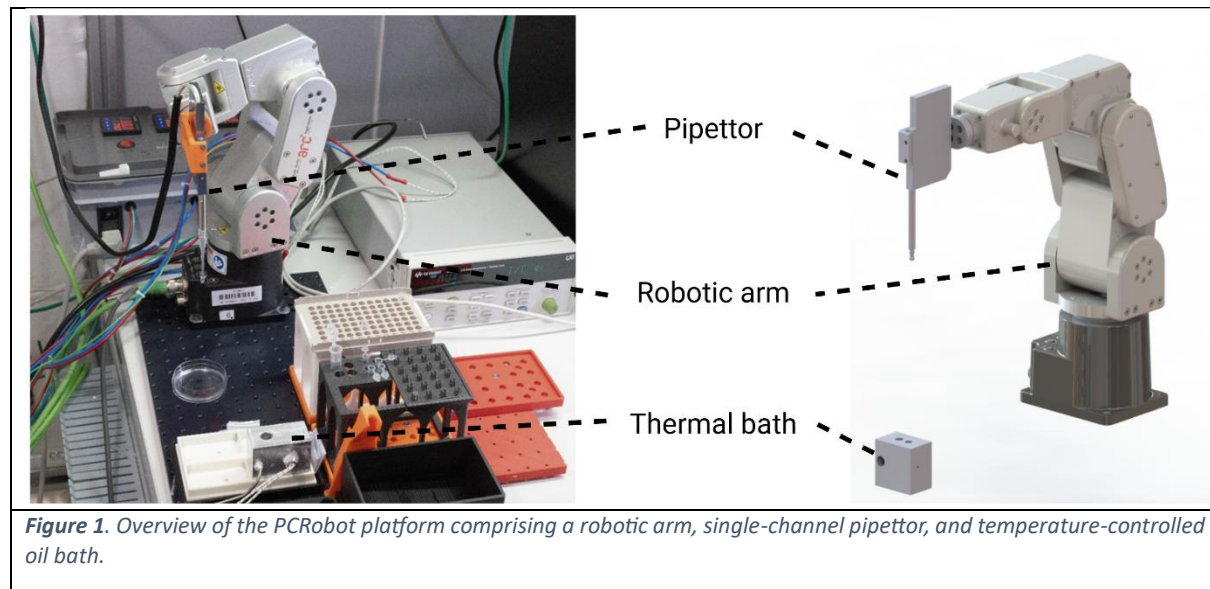
Amplification occurs entirely within sealed pipette tips, with temperature plateaus controlled by modulating immersion duration rather than complex thermal hardware. This architecture eliminates contamination-prone transfers, enables quantitative sample recovery, and reduces mechanical complexity, equipment redundancy, and consumable waste. The efficient heat transfer from direct oil-to-sample contact, combined with compatibility with standard robotic infrastructure, yields a scalable, automation-ready amplification platform.

Using DNA-encoded datasets, we demonstrate that PCRobot achieves amplification performance comparable to conventional automated workflows while reducing contamination risk and eliminating redundant instrumentation. By embedding thermal cycling directly within robotic operations, PCRobot represents a paradigm shift toward fully integrated, autonomous DNA data storage systems optimized for archival deployment.

Results and Discussions

PCRobot: Robotic liquid handling integrated with thermal cycling.

We developed an automated amplification platform designed for integration into end-to-end DNA data storage workflows (Fig. 1). The system combines a robotic arm-mounted pipettor for liquid handling (mixing, dispensing) with in-tip thermal cycling. Reagents (primers, template DNA, PCR master mix) are mixed through automated pipetting, but rather than transferring the mixture to PCR tubes for amplification in a separate thermocycler, the reaction mixture remains in the pipette tip, which serves as a high surface-to-volume ratio reaction vessel. Temperature cycling is achieved by immersing the tip in a heated oil bath (heating) and withdrawing it into ambient air (cooling).



Our approach revisits early PCR protocols that employed manual tube transfers between temperature-controlled water baths for denaturation, annealing, and extension. Although we initially tested a three-bath configuration (Supplementary Material and Fig. S1), we adopted a simpler single-bath design maintained above the highest target temperature. Temperature plateaus are achieved using pulse-

width modulation: the tip undergoes repetitive immersion and withdrawal cycles to maintain target temperatures, producing characteristic oscillations around setpoints (Fig. 2). Temperature monitoring employed a custom thermocouple assembly (detailed below in "Mock pipette with thermocouple for *in-situ* characterization"). Both duty cycle (immersion/withdrawal time ratio) and immersion depth can be modulated to control temperature. Based on measured thermocycler thermal tolerances (Fig. S2), we optimized the protocol to maintain temperature plateaus within ± 2 °C.

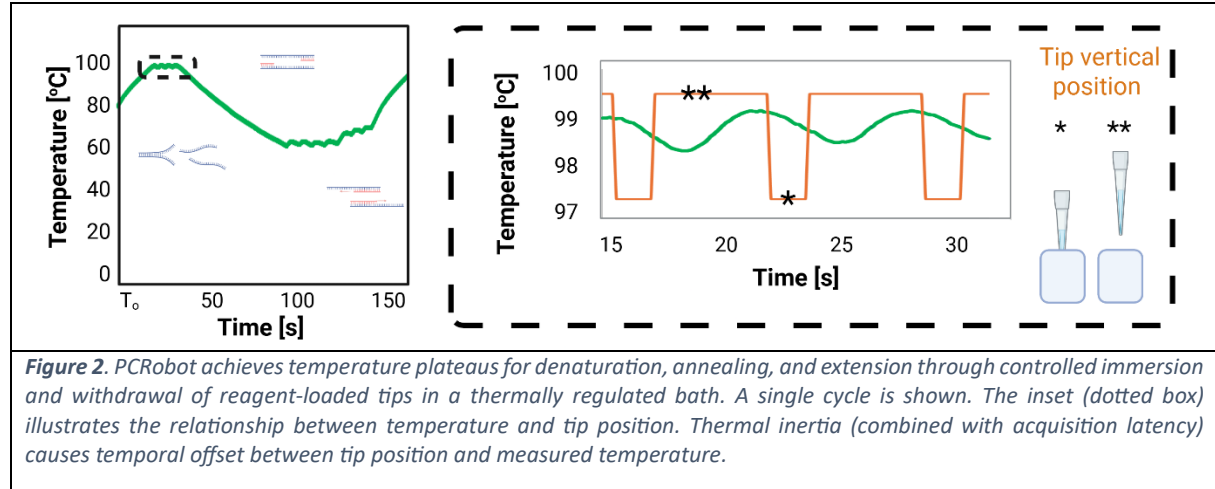
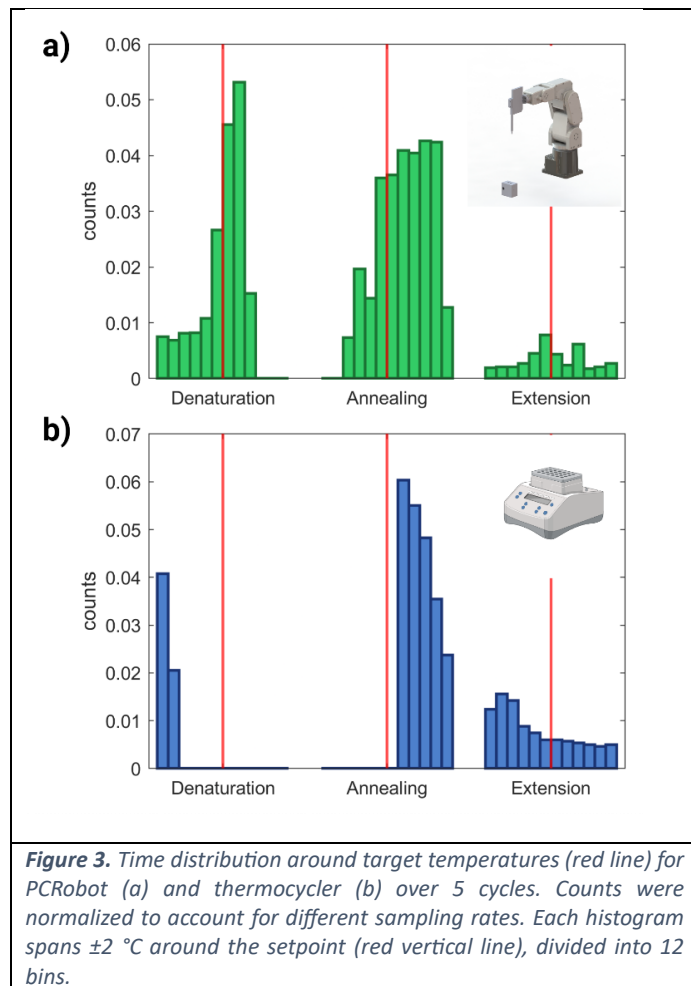


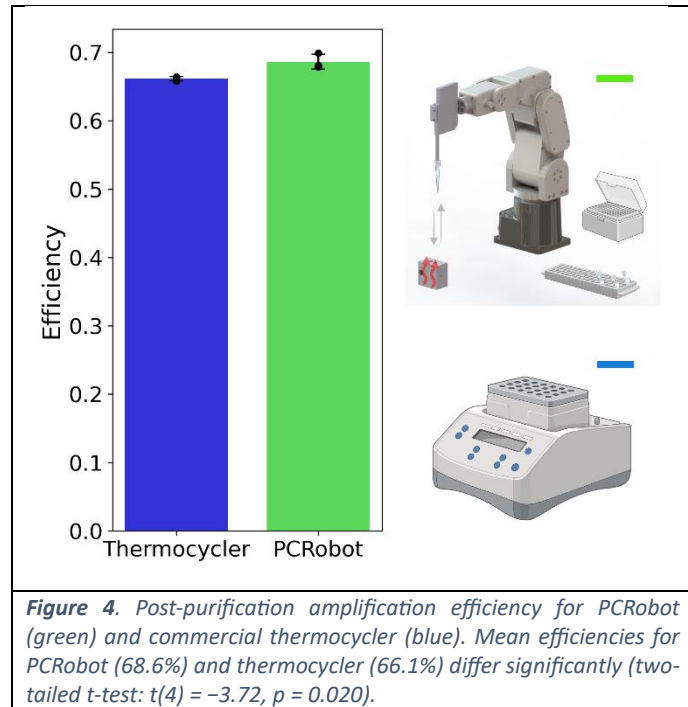
Figure 3 compares time distributions around target temperature plateaus (red lines) for PCRobot and a conventional thermocycler. Counts were normalized over 5 cycles to account for different sampling rates. Both systems show comparable performance, although PCRobot demonstrates higher accuracy (particularly for annealing) but slightly reduced precision. Broader temperature dispersion during the extension step results from limited robot speed, which prevents rapid tip withdrawal. This was partially mitigated by reducing immersion depth to compensate for thermal inertia.

To minimize footprint while maintaining autonomy, the MECA500 robot and Seyonic single-channel pipettor—connected via a custom holder—are assembled on a 30 × 30 cm breadboard integrating holders for consumables: tip rack, tubes (10×), custom sealing caps (24×; see "Sealing to retain liquids during thermal cycling"), and waste receptacle (Fig. 1 and Fig. S3).



Amplification efficiency comparable to commercial thermocycler.

We compared the amplification results of the PCRobot to a commercial thermocycler, under identical conditions: 20 μL reaction, 25 cycles. Post-purification DNA concentrations differed significantly between PCRobot (21.6 ng/mL) and the conventional thermocycler (13.1 ng/mL; two-tailed t-test: $t(4) = -3.07$, $p = 0.037$). However, amplification efficiency (E), defined in $C_n = C_0(1 + E)^n$, with C_0 , the initial concentration, C_n , the concentration after n cycles, provides a more appropriate comparison metric. PCRobot demonstrated significantly higher amplification efficiency (0.686 ± 0.011 , $n = 3$) compared to the thermocycler (0.662 ± 0.003 , $n = 3$; $t(4) = -3.72$, $p = 0.020$). This difference, while statistically significant, is marginal in practical terms as shown in Figure 4. Electropherograms confirmed that expected PCR products (amplicons) were equivalent for both systems (Fig. S4).



Thermal efficiency and process time optimisation.

While PCRobot achieves heating performance comparable to commercial thermocyclers through direct oil bath contact, it is outperformed during cooling (Fig. 5). For 25 cycles, the thermocycler requires approximately 30 minutes versus over 60 minutes for PCRobot. This difference arises because PCRobot relies on passive air convection, whereas thermocyclers employ active cooling. Despite the longer processing time, PCRobot's energy consumption (0.054 kWh), as measured by a power meter, is only marginally higher than that of the thermocycler (0.043 kWh). This is attributable to the fact that PCRobot integrates a robot, a pipettor, and a thermostated bath. Moreover, a fair comparison would require inclusion of the robot used for loading samples into the thermocycler.

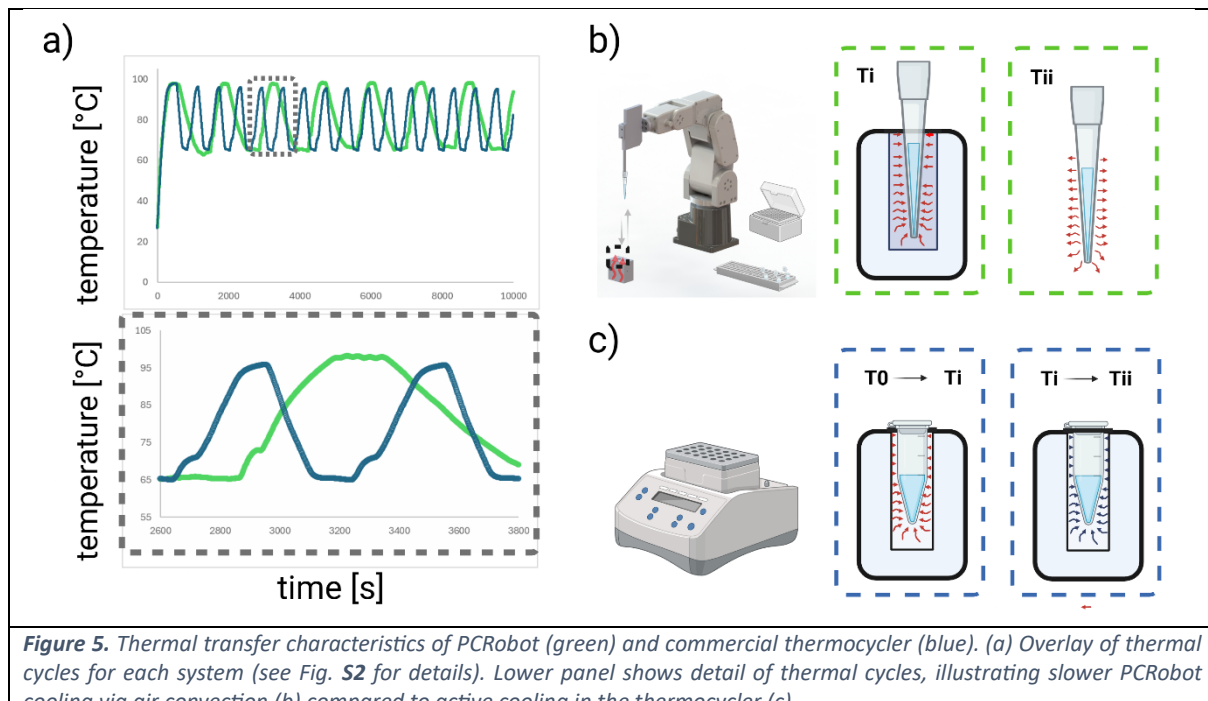


Figure 5. Thermal transfer characteristics of PCRobot (green) and commercial thermocycler (blue). (a) Overlay of thermal cycles for each system (see Fig. S2 for details). Lower panel shows detail of thermal cycles, illustrating slower PCRobot cooling via air convection (b) compared to active cooling in the thermocycler (c).

Although timing is not critical for archival DNA data storage, other applications may benefit from reduced cycle times. Using a three-bath configuration with a faster XYZ robotic platform, we achieved 20 cycles in 22 minutes (Supplementary Fig. S1c). Further reduction could be achieved by adding a fourth temperature-controlled bath below the lowest target temperature. First order impulse response measurements, $T(t) = T_1 + (T_0 - T_1)(e^{-t/\tau})$, quantified cooling in ambient air (24°C) versus a regulated bath (51°C). The time constant τ decreased respectively from 43s to 6s when cooling from 96°C to 54°C (see SM; Figure S5 and Table S1 for details). While this represents substantial time savings, it would increase system complexity, requiring additional baths, thermal controllers, and robotic steps.

An alternative approach to improve thermal transfer would be reducing tip wall thickness. Although implementation is beyond the current scope, we evaluated potential benefits by measuring the instantaneous inverse thermal time constant ($1/\tau$) for tips versus PCR tubes immersed in a heated bath (see Methods). PCR tube walls (0.3 mm) are half the thickness of standard tips (0.6 mm). Figure 6 shows that PCR tubes exhibited consistently higher $1/\tau$ values, demonstrating substantially faster thermal equilibration. Both vessels displayed non-monotonic temperature dependence: $1/\tau$ increased at lower temperatures, peaked around 40–45 °C, and decreased at higher temperatures. This trend reflects temperature-dependent water properties (viscosity, thermal conductivity) and potential boundary-layer effects at the vessel–fluid interface. Importantly, the relative offset between curves remained consistent across the temperature range, indicating that geometry and wall thickness dominate thermal time constants under these conditions. Since experiments used 5 µL volumes to maintain constant surface-to-volume ratios (within 10%), the thermal advantage is attributed to favorable PCR tube wall thickness.

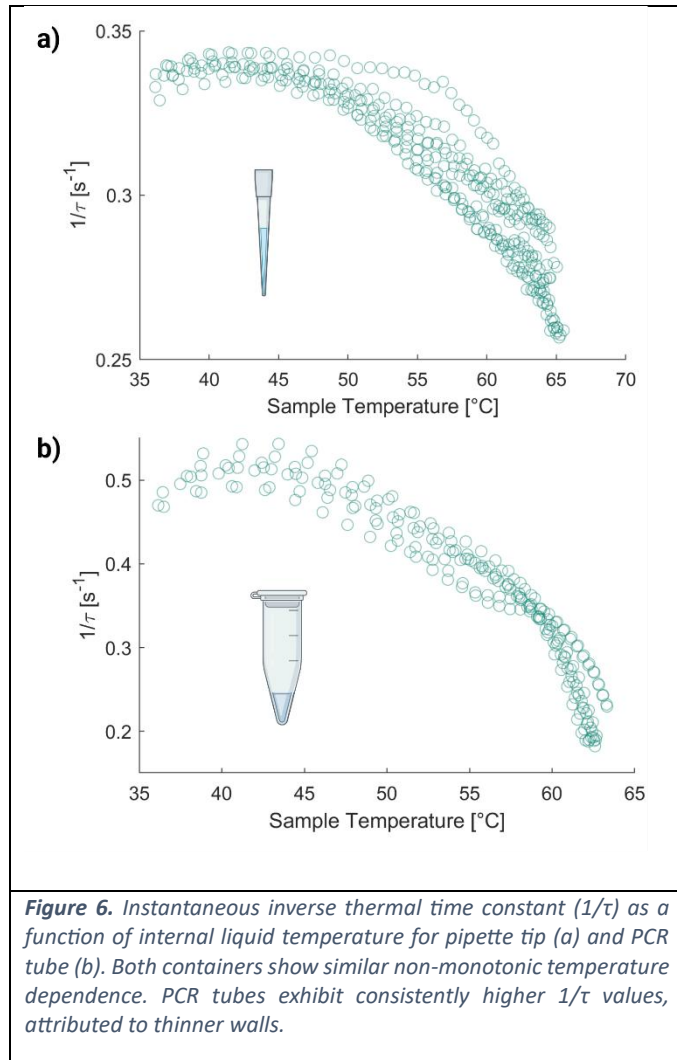


Figure 6. Instantaneous inverse thermal time constant ($1/\tau$) as a function of internal liquid temperature for pipette tip (a) and PCR tube (b). Both containers show similar non-monotonic temperature dependence. PCR tubes exhibit consistently higher $1/\tau$ values, attributed to thinner walls.

Mock pipette with thermocouple for in-situ characterisation.

Miniaturized Type-K thermocouple junctions were fabricated through controlled micro-fusion of fine-gauge Chromel-Alumel wires, yielding low-thermal-mass sensors for localized temperature measurements (Fig. S6 and Methods). These were integrated into a mock mandrel designed to replicate Seyonic single-channel pipettor dimensions. The same thermocouple junctions characterized laboratory thermocyclers for comparison and to establish target temperature tolerances (Fig. S2).

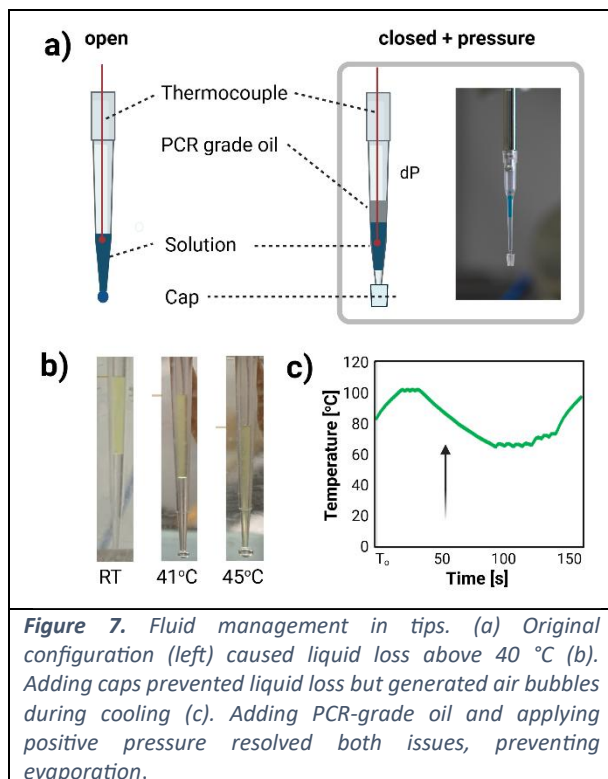
Extensive design iterations ensured reliable tip insertion and air-tight sealing. The final design employs a shortened mandrel with friction fit using two O-rings. O-rings compensate for relatively rough 3D-printed surfaces, ensuring proper tip sealing. The shortened design reduces displaced air volume during tip insertion, lowering initial internal pressure and preventing tip detachment during thermal cycling.

Sealing tips to retain liquids during thermal cycling.

Initial PCRobot evaluation revealed that regardless of tip type or volume, liquid retained during pipetting at ambient temperature was expelled above 40 $^{\circ}\text{C}$ (Fig. 7a). We systematically investigated this phenomenon. Our initial hypothesis—thermal expansion of fluids (solution and trapped air)—could not fully explain liquid loss (Supplementary Material and Fig. S7). The most likely cause is

combined thermal expansion with temperature-dependent changes in surface tension^{26–28} and viscosity²⁹, both of which decrease with temperature and negatively impact liquid retention.

We addressed this by sealing tips with elastomeric caps during thermal cycling. We designed and fabricated injection-moulded elastomeric caps (Fig. 7d and Fig. S8). During operation, the robot automatically retrieves caps before amplification and removes them 30 seconds after the final cycle, ensuring temperature drops below 40 °C to prevent heat-related liquid loss.



This approach achieved complete liquid retention over 25 PCR cycles. However, air bubbles formed systematically during transitions from denaturation (96 °C) to annealing (74 °C), indicating that rapid thermal expansion and contraction generate bubbles even with degassed solutions (Fig. 7c). When liquid was fully submerged in the bath, bubble formation interfered with thermal measurements and process optimization. Additionally, liquid evaporation occurred inside tips. We addressed both issues by overlaying PCR-grade oil on the reaction mixture and applying positive pressure (1200 mbar) during operation. This optimized configuration maintained stable conditions over 25 cycles (Fig. 7a).

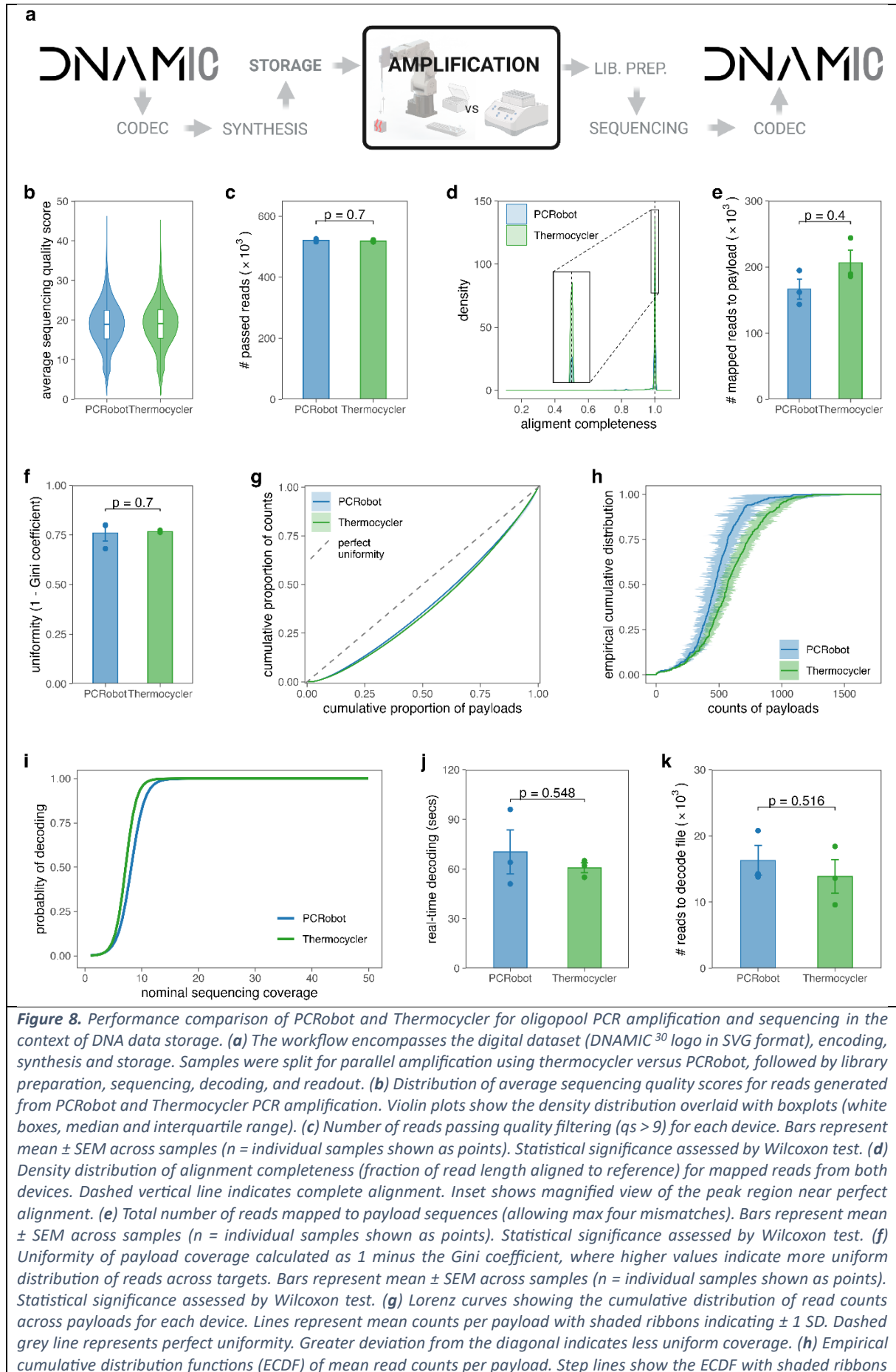
Validation for DNA data archival workflows

We validated the automation-compatible amplification system within a DNA data storage workflow using Oxford Nanopore Technologies (ONT) sequencing. The validation dataset consisted of the DNAMIC logo³⁰ encoded in SVG format, encapsulated in an Open Archival Information System (OAIS, ISO 14721)-compliant OLOS package³¹ (Fig. 8a). The file (8.1 kB) was encoded using a custom codec (Supplementary Materials and Fig. S9), incorporating 30% Reed–Solomon error-correction redundancy, yielding 352 oligonucleotides (243 nt each). Each oligonucleotide contained 18-nt forward and reverse primers flanking a 207-nt data payload, designed according to thermodynamic and hybridization constraints to ensure amplification efficiency and primer orthogonality.

Amplification of the encoded oligonucleotide pool was performed using both a standard thermocycler and PCRobot under identical cycle numbers and reaction compositions. Following amplification, ONT library preparation and sequencing were performed. Sequencing reads were aligned to the reference oligonucleotide library to assess amplification uniformity, yield, and fidelity.

Nanopore sequencing reveals comparable amplification uniformity between PCRobot and thermocycler.

Next, we compare multiple quality metrics for multiplex amplification and sequencing between platforms. Read quality scores were similarly high, with median values around 20 for both PCRobot and thermocycler (Fig. 8b). The number of reads passing quality filtering ($qs > 9$) showed no significant difference (Wilcoxon test, $p > 0.05$; Fig. 8c), indicating PCRobot does not compromise sequencing data quality. Alignment completeness, measured as the fraction of read length mapped to reference sequences, displayed nearly identical distributions, with most reads achieving complete alignment (Fig. 8d). Total reads mapped to payload sequences did not differ significantly between platforms (Wilcoxon test, $p > 0.05$; Fig. 8e). Coverage uniformity across payloads, quantified using the Gini coefficient, revealed no significant difference in amplification bias (Wilcoxon test, $p > 0.05$; Fig. 8f). Lorenz curve analysis illustrated this equivalence, with both devices showing similar deviation from perfect uniformity (Fig. 8g). Empirical cumulative distribution of read counts per payload demonstrated comparable performance, with largely overlapping distributions indicating similar payload representation (Fig. 8h). Collectively, these results demonstrate that PCRobot performs equivalently to conventional thermocyclers for oligonucleotide pool PCR amplification, producing comparable data quality, yield, and target coverage uniformity.



representing ± 1 SEM. Higher curves indicate greater representation of payloads at a given count threshold. (i) Probability of successful decoding as a function of nominal sequencing coverage for PCRobot and Thermocycler samples. Lines represent generalized linear model fits (quasibinomial) showing the relationship between raw sequencing coverage and decoding success rate for each device. (j) Real-time decoding latency measured as the time interval (in seconds) between sequencing initiation and successful decoding. Bars represent mean \pm SEM across samples (n = individual samples shown as points). Statistical significance assessed by two-sided t-test. (k) Number of sequencing reads required to successfully decode the encoded message in real time. Bars represent mean \pm SEM across samples (n = individual samples shown as points). Statistical significance assessed by two-sided t-test. All data represent biological replicates with PCRobot (blue) and Thermocycler (green) conditions. P-values in panels c, e, and f are from two-sided Wilcoxon rank-sum tests.

File decoding performance is comparable between PCRobot and thermocycler.

To assess whether PCR platform choice affects data decoding, we evaluated real-time decoding performance for samples amplified using PCRobot versus thermocycler. Probability of successful decoding as a function of nominal sequencing coverage showed similar trends for both devices, with success increasing with coverage depth (Fig. 8i). Generalized linear modeling revealed that decoding success saturated (10/10 successful decodings from random sampling) at approximately 10 \times coverage for thermocycler and approximately 12 \times coverage for PCRobot, indicating slightly higher coverage requirements for consistent decoding with the automated platform. Real-time decoding latency, measured as the time interval between sequencing start and successful decoding, showed no significant difference between platforms (t-test, $p > 0.05$; Fig. 8j), although PCRobot exhibited a slight trend toward longer decoding times. Similarly, the number of sequencing reads required for successful decoding did not differ significantly between PCRobot and thermocycler (t-test, $p > 0.05$; Fig. 10c), despite a modest trend toward higher read requirements for PCRobot samples.

Conclusions

Robotics and automation are transforming molecular workflows in life sciences, not merely by increasing throughput but by enabling fundamental reconsideration of how core biochemical processes are implemented. Rather than replicating established laboratory practices, automation provides an opportunity to redesign protocols for robustness, integration, and sustainability. Here, we applied this paradigm to PCR amplification by revisiting water bath–based thermal cycling and integrating it directly within a robotic platform.

PCRobot implements thermal cycling as a robotic operation through controlled immersion and withdrawal of sealed pipette tips in a single temperature-controlled bath. Evaluation using DNA-encoded datasets demonstrates that this architecture preserves the essential molecular properties required for DNA data storage—reliable amplification, uniform representation of encoded sequences, and sequencing fidelity—at levels equivalent to conventional thermocycler workflows.

Importantly, PCRobot transforms conventional PCR performance metrics into intrinsic system properties. Contamination control is achieved structurally through sealed-tip amplification and elimination of inter-instrument transfers, rather than procedural safeguards. Automation compatibility emerges from embedding thermal cycling within the same robotic infrastructure used for liquid handling, eliminating dedicated thermocyclers and associated mechanical interfaces. Energy efficiency results from simplified thermal management—a single heated bath with passive cooling—rather than actively controlled thermal blocks, reducing hardware complexity.

More broadly, this work demonstrates how reframing molecular biology protocols as components of integrated automated systems can yield architectures that are functionally equivalent at the biochemical level while superior at the system level. This approach may inform redesign of other core molecular operations as life sciences transition toward autonomous, distributed, and archival-scale technological platforms.

Methods

Smart Pipettor:

Pipettor: We used a Single Channel Pipettor (PCNC-0061-00) from Seyonic SA with a System Controller Dual Pressure/Vacuum Source (Model PCNC-0071-00) for ultra-precise pipetting. The pipetting system is operated remotely via TCP/IP. For the **robotic unit**, we used the Meca500, a compact six-axis industrial robotic arm from Mecademic. It has a reach of 330 mm and a payload capacity of 0.5 kg. The unit was fixed to a 300x300x10 mm breadboard that also accommodated 3D printed parts for supplies and waste. The robot was connected to the pipettor using a custom-made 3D printed holder. **3D printing** was performed using a Prusa mk3s FDM (Fused Deposition Modeling) printers and 1.75 mm PLA filaments from Form Futura. **Control software.** We use the Synapxis integrated development environment (IDE) and control interface to control, which supports both TCP/IP and serial communication, to control the robot and pipettor. A dedicated script (available in Annex) was developed for the occasion.

The **mock pipette** was designed to be reliably printed on an MSLA 3D printer. To maximize geometric accuracy along the radial axes, the mock pipette parts are printed vertically. To limit the risk of a part unsticking from the print plate, the mock pipette was split into four parts, the mandrel, two “half arms” and one fixation. The parts are connected via a crescent shaped connector, to limit degrees of freedom during construction. The mandrel features a through-hole for the passage of the thermocouple. When connected to the half-arm, the crescent shaped connector leaves a gap between the two parts, allowing the passage of the thermocouple.

Thermocouples fabrication. Miniature thermocouple junctions were produced using fine-gauge, commercially available Type-K thermocouple wire (Chromel-Alumel; conductor cross-section 0.05 mm²). The two conductors were gently twisted at the distal end to ensure mechanical alignment prior to junction formation. Electrical energy was delivered via a low-voltage laboratory power supply equipped with an output-side capacitive buffer (five electrolytic capacitors, nominal total capacitance \approx 1 mF). The positive terminal was contacted through a graphite element wrapped in copper tape, while the negative terminal interfaced with the thermocouple leads through screw-type contacts.

Junction formation occurred when the twisted wire pair was momentarily brought into contact with the graphite element. The localized resistive heating at the contact point promoted rapid melting and fusion of the alloy pair, forming a stable thermo-electric junction. The resulting junctions were visually inspected and tested for electrical continuity and thermal response.

Thermal transfer efficiency. Thermal response dynamics of the pipette tip and PCR tubes were quantified during repeated immersion into a thermostated water bath, heated to 71°C and magnetically stirred to ensure spatially uniform temperature. A mock pipette mounted on the robot performed controlled immersion-withdrawal cycles, dipping each vessel to a fixed depth and dwell time. A miniature thermocouple was inserted into the liquid contained within each vessel to monitor the internal temperature, while a second thermocouple positioned adjacent to the immersion point recorded the bath temperature. Both channels were logged at high temporal resolution ($\Delta T= 0.15$ s).

Temperature traces were pre-processed to exclude artefactual points (e.g., transitions between air and water). The instantaneous derivative of internal temperature, dT_{sample}/dt , was obtained numerically. Assuming a lumped-capacitance model, the instantaneous inverse thermal time constant was computed as

$$\frac{1}{\tau}(t) = \frac{dT_{\text{sample}}/dt}{T_{\text{bath}} - T_{\text{sample}}},$$

which reflects the effective heat-transfer rate between the bath and the liquid inside the vessel. The resulting $1/\tau$ values were plotted against the instantaneous internal temperature for each geometry.

Elastomeric caps were fabricated by injection moulding using an *Arburg Allrounder S170* injection press. The selected material was Santoprene™ thermoplastic vulcanizate (TPV), belonging to the thermoplastic elastomer (TPE) family. Prior to injection, the material was dried at 80 °C for 3 hours to eliminate residual moisture. Injection moulding was performed under the following processing parameters: material temperature of 190 °C, mould temperature regulated at 80 °C, and an injected volume of 0.5 cm³ per cycle. The maximum injection pressure was set at 400 bar, and the cycle time was approximately 10 seconds. The mould was designed to ensure uniform filling and consistent part geometry under these thermal and pressure conditions. After ejection, the moulded caps were allowed to cool to ambient temperature before further handling or characterization. All fabrication runs were performed under identical process conditions to ensure reproducibility.

DNA data:

Materials/synthesis

DNA Encoding. The DNAMIC logo (SVG format, 8.1 kB) was encoded into DNA using the OLOS package with 30% error-correction redundancy, yielding 352 oligonucleotides (oligos). Each oligo comprised 243 nt, including 18-nt forward and reverse primer binding sites flanking a 207-nt data payload. Primer sequences were generated via SHA-256 hashing and selected based on Gibbs free energy, melting temperature difference (< 2 °C), and a Hamming distance > 10 to minimize cross-hybridization. The oligo pool was obtained from TWIST Bioscience and primers from Eurofins, additional primers were synthesised using the Kilobaser 1 synthesiser (Mabeal).

Data Structure and Encoding Scheme. Input files were converted into an $n \times m$ matrix, where $n = 34$ (equivalent to 153 nts) and m was determined by dividing the file length by 34. Incomplete columns were filled with dummy data generated by a modulo-256 counter to prevent repeating patterns; if m was odd, one column was added. Each sequence included a 4-byte index for positional identification, allowing encoding of files up to 146 GB.

Error Correction and DNA Conversion. Error correction employed Reed–Solomon (RS) codes at two levels: inner codes (8 bytes per column) and outer codes (calculated for each row joining two bytes). Redundancy ratios (r) were set between 10–30% based on nanopore sequencing performance. Each symbol represented 16 bits encoded by 9 nucleotides using a GF(41) codon wheel ($256^2 \rightarrow 41^3$ base conversion), ensuring that no base was repeated more than three times.

Thermal cycling PCR amplification was carried out using the Q5 High-Fidelity DNA Polymerase kit (M0491S; New England Biolabs), following the manufacturer's protocol. Reactions (25 µL final volume) contained template DNA in the nanogram range, forward and reverse primers (10 µM stocks), and the supplied Q5 buffer and dNTPs, with nuclease-free water added to standardize volume. Reactions prepared with M0491S were assembled on ice, as recommended. Because M0494S provides the same

Q5 polymerase in a ready-to-use master mix that does not require cold-setup, it represents a fully compatible formulation and will be adopted for future experiments.

Thermal cycling consisted of an initial denaturation at 98 °C for approximately 30 s, followed by cycles including brief denaturation (~10 s at 98 °C), annealing (~15 s at 65 °C), and short extension (~5 s at 72 °C), with a final elongation step of ~2 min at 72 °C. These parameters were optimized for the DNAMIC_Logo amplicon and are consistent with manufacturer recommendations for short, high-fidelity targets. Amplicons were evaluated by agarose gel electrophoresis to confirm fragment length and specificity.

The protocol was carried out using the PCRobot and Bio-Gener (Labgene) thermocycler, additional amplification was performed on the MiniOne® PCR system thermocycler (The MiniOne, 2025).

Purification with MagSi DNA-mf magnetic silica beads. All steps were performed at room temperature (20–25 °C) using low-bind plasticware and nuclease-free water. *Bead equilibration.* The MagSi DNA-mf bead suspension (silica-based magnetic particles) was homogenized by gentle inversion. An aliquot of 50 µL bead suspension was transferred to a 1.5 mL tube, mixed with 50 µL nuclease-free water, briefly pipette-mixed, and placed on a magnetic rack until the supernatant cleared (~1–2 min). The supernatant was discarded and the equilibration wash was repeated 3 times. *DNA binding.* To the equilibrated beads, 100 µL of “prepared binding buffer” was added and mixed by pipetting. The prepared binding buffer consisted of 20% (v/v) of a stock binding buffer—4 M guanidinium chloride, 40 mM Tris-HCl, 17.6 mM EDTA, pH 8.0 (adjusted with HCl)—diluted in 80% (v/v) isopropanol. Next, 10 µL of sample was dispensed directly into the liquid phase without dislodging the bead pellet or aspirating beads. The tube was vortexed at high speed for 2 min, then placed on the magnet until clear; the supernatant was discarded. *Wash.* A 100 µL wash was performed by carefully adding wash solution over the pellet to avoid disturbing it; the wash solution consisted of 10 mM Tris-HCl, 1 mM EDTA in 80% (v/v) ethanol, pH 8.0. The tube was returned to the magnet and the supernatant was removed. The ethanol wash was repeated (see note below on repeats). *Drying.* Tubes were left open to air-dry the bead pellet for 15 min to evaporate residual ethanol. *Elution.* 20 µL nuclease-free water was added, the tube was shaken for 2 min to resuspend the beads, then placed on the magnet and the eluate was collected into a fresh tube. DNA was stored at –20 °C.

Quality control. Amplified DNA oligo pools were quantified using Qubit dsDNA High Sensitivity reagents (Thermo Fisher Scientific), and amplicon size distributions were assessed on an TapeStation 2200 (Agilent) with D1000 ScreenTape.

ONT nanopore library preparation and sequencing. For each amplified and quality-controlled oligo-pool sample (thermal cycler, n = 3; PCRobot, n = 3), 250 fmol of purified amplicon DNA was used for ONT library preparation following the high-performance protocol ⁸. Full protocol is available at protocols.io (dx.doi.org/10.17504/protocols.io.dm6gp973jvzp/v2). Sequencing was performed on a MinION Mk1B (ONT) using an R10.4.1 MinION flow cell. To obtain comparable sequencing depth across all six libraries, each run was stopped after reaching approximately 5.5×10⁵ reads per sample, yielding ~1,563× nominal coverage. The flow cell was washed and reused between runs according to the manufacturer’s instructions. Raw signal data collected in POD5 format was basecalled with Dorado v1.1.1 using the simplex SUP model (dna_r10.4.1_e8.2_400bps_sup@v5.2.0).

Bioinformatic sequencing analysis. The resulting sequences in uBAM files were categorized into “passed” or “failed” based on their average quality scores (q-scores), only reads with q-scores above or equal to the threshold of 9 were included in subsequent downstream processing. The reads in uBAMs were converted to FASTQ files using samtools (vX) and trimmed for adapters using cutadapt (v5.1) with the following parameters: cutadapt -e 0.04 -g

ACGAGCGTGAGTACTCTG...CACCGACTGGAGCTGGCG --action=retain --revcomp -m 235 -M 255. Trimmed reads were then mapped to the reference payload sequences using minimap2 (v2.30) with the following parameters: minimap2 -ax sr -L --MD -t8 -Y -eqx -k10 -w5 -m10 --secondary=yes. Data analysis and visualization were performed using custom Python and R scripts.

Real-time decoding. To leverage ONT nanopore sequencing's real-time read output, a Python 3 application with a node-based architecture was developed for real-time decoding. The application monitors MinKNOW's continuous output for newly written raw-read batches, submits each batch to the decoding pipeline, and upon successful decoding, signals MinKNOW via its API to terminate the run. The software is modular (file monitoring, read quality-control, decoding [see Methods], API client) and processes sequential read batches to minimize latency. Batch size of 350 reads was used in this experiment that approximately corresponds to 1X of nominal coverage of the given oligo pool. Implementation details and source code can be provided upon reasonable request.

Code availability.

The codec is available in Gitlab: <https://gitlab.unige.ch/dnamic/unige-dna-codec/-/tree/pyb>. The code used for DNA data analysis is available in Github: <https://github.com/genomika-lt/PCRobot>

Contributions

VB, JG: Investigation, Formal Analysis, Data Curation, Validation and Methodology. SJ, KK, LŽ, DK, IG: Investigation, Methodology, Validation, Data curation. PYB: Investigation, Methodology, Validation. SW, VR, SA, PN: Investigation, Methodology. BVDS, AC: Resources, Data curation. MJ: Resources, Funding Acquisition. RR, TH: Funding Acquisition. JC: Conceptualisation, Supervision, Formal analysis, Validation, Writing – original draft, Funding acquisition. All authors: Writing – review & editing.

Acknowledgements

We would like to thank Frédéric Flahaut and Duygucan Güл for support on injection moulding and molecular biology respectively. We would like to thank Friedrich Simmel for his contribution to funding acquisition. This research was funded by the European Innovation Council Pathfinder Program, under the project DNAMIC (DNA Microfactory for Autonomous Archiving), Grant Agreement No. 101115389 and Swiss State Secretariat for Education, Research and Innovation (SERI) under contracts number 23.00300 and 23.00487.

References

1. Reinsel, D., Gantz, J. & Rydning, J. The Digitization of the World - From Edge to Core. IDC White Paper. *IDC White Paper* 20, 3 (2018).
2. Church, G. M., Gao, Y. & Kosuri, S. Next-generation digital information storage in DNA. *Science* (1979) 337, 1628 (2012).
3. Goldman, N. *et al.* Towards practical, high-capacity, low-maintenance information storage in synthesized DNA. *Nature* 2013 494:7435 494, 77–80 (2013).
4. Grass, R. N., Heckel, R., Puddu, M., Paunescu, D. & Stark, W. J. Robust chemical preservation of digital information on DNA in silica with error-correcting codes. *Angewandte Chemie - International Edition* 54, 2552–2555 (2015).
5. Organick, L. *et al.* Random access in large-scale DNA data storage. *Nat Biotechnol* 36, 242–248 (2018).
6. Ceze, L., Nivala, J. & Strauss, K. Molecular digital data storage using DNA. *Nature Reviews Genetics* 2019 20:8 20, 456–466 (2019).
7. Antkowiak, P. L. *et al.* Low cost DNA data storage using photolithographic synthesis and advanced information reconstruction and error correction. *Nat Commun* 11, 5345- (2020).
8. Žemaitis, L. *et al.* High-performance protocol for ultra-short DNA sequencing using Oxford Nanopore Technology (ONT). *PLoS One* 20, e0318040 (2025).
9. Chen, Y. J. *et al.* Quantifying molecular bias in DNA data storage. *Nature Communications* 2020 11:1 11, 3264- (2020).
10. Press, W. H., Hawkins, J. A., Schaub, J. M., Schaub, J. M. & Finkelstein, I. J. HEDGES error-correcting code for DNA storage corrects indels and allows sequence constraints. *Proc Natl Acad Sci U S A* 117, 18489–18496 (2020).
11. Mullis, K. B. The unusual origin of the polymerase chain reaction. *Sci Am* 262, (1990).
12. Saiki, R. K. *et al.* Enzymatic amplification of β -globin genomic sequences and restriction site analysis for diagnosis of sickle cell anemia. *Science* (1979) 230, (1985).
13. Cheng, J. *et al.* Implementation of Rapid Nucleic Acid Amplification Based on the Super Large Thermoelectric Cooler Rapid Temperature Rise and Fall Heating Module. *Biosensors* 2024, Vol. 14, Page 379 14, 379 (2024).
14. Wittwer, C. T., Fillmore, G. C. & Hillyard, D. R. Automated polymerase chain reaction in capillary tubes with hot air. *Nucleic Acids Res* 17, (1989).
15. Ahrberg, C. D., Manz, A. & Chung, B. G. Polymerase chain reaction in microfluidic devices. *Lab Chip* 16, (2016).
16. Zhang, Y. & Ozdemir, P. Microfluidic DNA amplification-A review. *Anal Chim Acta* 638, 115–125 (2009).

17. Charmet, J., Arosio, P. & Knowles, T. P. J. Microfluidics for Protein Biophysics. *J Mol Biol* 430, 565–580 (2018).
18. Huggett, J. F. *et al.* The digital MIQE guidelines: Minimum information for publication of quantitative digital PCR experiments. *Clin Chem* 59, (2013).
19. Hindson, B. J. *et al.* High-throughput droplet digital PCR system for absolute quantitation of DNA copy number. *Anal Chem* 83, (2011).
20. Basu, A. S. Digital Assays Part I: Partitioning Statistics and Digital PCR. *SLAS Technology* vol. 22 Preprint at <https://doi.org/10.1177/2472630317705680> (2017).
21. Whitesides, G. M. The origins and the future of microfluidics. *Nature* vol. 442 Preprint at <https://doi.org/10.1038/nature05058> (2006).
22. Squires, T. M. & Quake, S. R. Microfluidics: Fluid physics at the nanoliter scale. *Rev Mod Phys* 77, (2005).
23. OT-2 Liquid Handler | Opentrons Lab Automation from \$10,000 | Opentrons. <https://opentrons.com/robots/ot-2#resources>.
24. Bajar, B. T., Wang, E. S., Zhang, S., Lin, M. Z. & Chu, J. A guide to fluorescent protein FRET pairs. *Sensors (Switzerland)* vol. 16 Preprint at <https://doi.org/10.3390/s16091488> (2016).
25. Gach, P. C., Iwai, K., Kim, P. W., Hillson, N. J. & Singh, A. K. Droplet microfluidics for synthetic biology. *Lab on a Chip* vol. 17 Preprint at <https://doi.org/10.1039/c7lc00576h> (2017).
26. Kalová, J. & Mareš, R. The temperature dependence of the surface tension of water. *AIP Conf Proc* 2047, 20007 (2018).
27. Mayer, S. W. Dependence of Surface Tension on Temperature. *J Chem Phys* 38, 1803–1808 (1963).
28. Kalová, J. & Mareš, R. Temperature Dependence of the Surface Tension of Water, Including the Supercooled Region. *International Journal of Thermophysics* 2022 43:10 43, 154- (2022).
29. Korson, L., Drost-Hansen, W. & Millero, F. J. Viscosity of water at various temperatures. *Journal of Physical Chemistry* 73, 34–39 (2002).
30. DNAMIC: DNA Microfactory for Data Archiving | EU Project. <https://dnamic.org/>.
31. OLOS: The Swiss solution for managing research data. <https://olos.swiss/>.

Supplementary Materials: High-fidelity robotic PCR amplification

Vincent Beguin^{1,*}, Jean Grétillat^{2,*}, Kornelija Kaminskaitė³, Simonas Juzenas³, Dainius Kirsnauskas³, Pierre-Yves Burgi⁴, Samuel Wenger¹, Valentin Remonnay¹, Silvia Angeloni¹, Patrick Neuenschwander¹, Bart van der Schoot⁵, Augustin Cerveaux⁵, Thomas Heinis⁶, Renaldas Raisutis⁷, Martin Jost⁸, Lukas Zemaitis³, Ignas Galminas^{3#}, Jérôme Charmet^{1,2,9#}

10. *School of Engineering–HE-Arc Ingénierie, HES-SO University of Applied Sciences Western Switzerland, Neuchâtel, Switzerland*

11. *School of Precision and Biomedical Engineering, University of Bern, Bern, Switzerland*

12. *Department of DNA data storage, Genomika, Kaunas, Lithuania*

13. *IT Department, University of Geneva, Geneva, Switzerland*

14. *Seyonic SA, Neuchâtel, Switzerland*

15. *Department of Computing, Imperial College London, London, United Kingdom*

16. *Ultrasound Research Institute, Kaunas University of Technology, Kaunas, Lithuania*

17. *MABEAL GmbH, Graz, Austria*

18. *Warwick Medical School, University of Warwick, Coventry, United Kingdom*

* the authors contributed equally to the work.

3-bath PCRobot.

Early implementations of the PCRobot relied on 3-bath container heated to the desired temperature plateaus, using hot plates (Figure S1). The Seyonic pipettor single head, attached to a 3-axis positioning system (OMNI UNIVERSAL ROBOT by Tecan, internal reference n°0103), moves from one bath to the next to perform PCR into the tip. The thermal response along with the position of the robot are shown in Figure S1a. Later we favoured the simple PCRobot implementation with a single bath and a robotic arm, as detailed in the manuscript. Early measurements were compared and validated using the MiniOne Kit (thermocycler and gel electrophoresis). The PCR amplification measurement was performed using the MiniOne dye added to the mix before dispensing on the gel for electrophoresis. Control experiments were performed using the MiniOne thermocycler (same conditions) followed by the same gel electrophoresis. Figure S1c shows the results that correspond to a 20-cycle process performed in 22 minutes for the PCRobot and in 15 minutes for the MiniOne thermocycler.

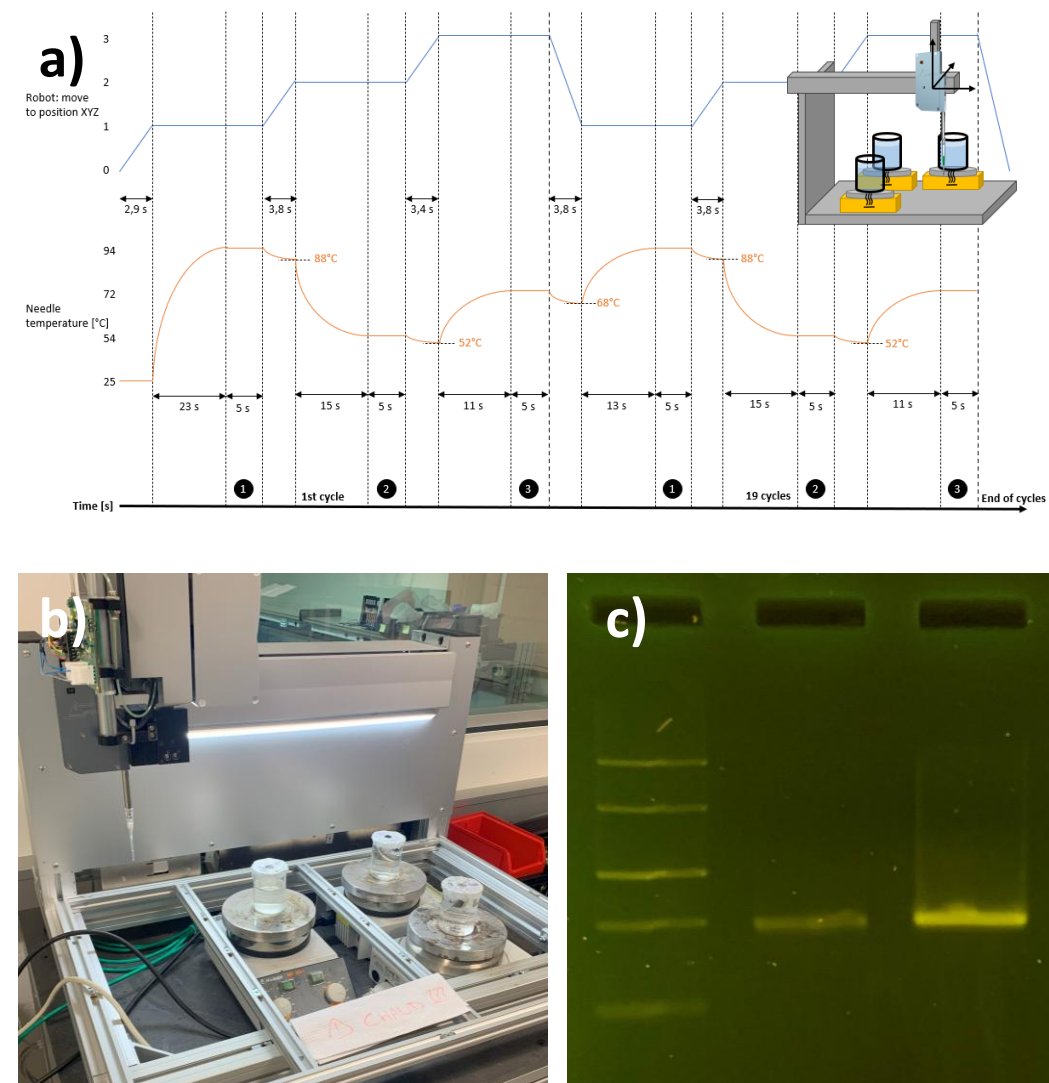


Figure S1. Three bath robotic-enable DNA amplification set-up. a) Temperature profile and corresponding robot position. Inset shows the principle. b) image of the set-up. c) Electropherogram (MiniOne kit) comparing the performance of the MiniOne thermocycler with the 3bath PCRobot device. Lane 1 - ladder, lanes 2 – MiniOne thermocycler: three replicate samples amplified using the MiniOne thermocycler; lanes 3 – PCRobot. The band visible across the lane corresponds to the expected PCR product (amplicon).

Thermal response of the thermocycler and PCRobot.

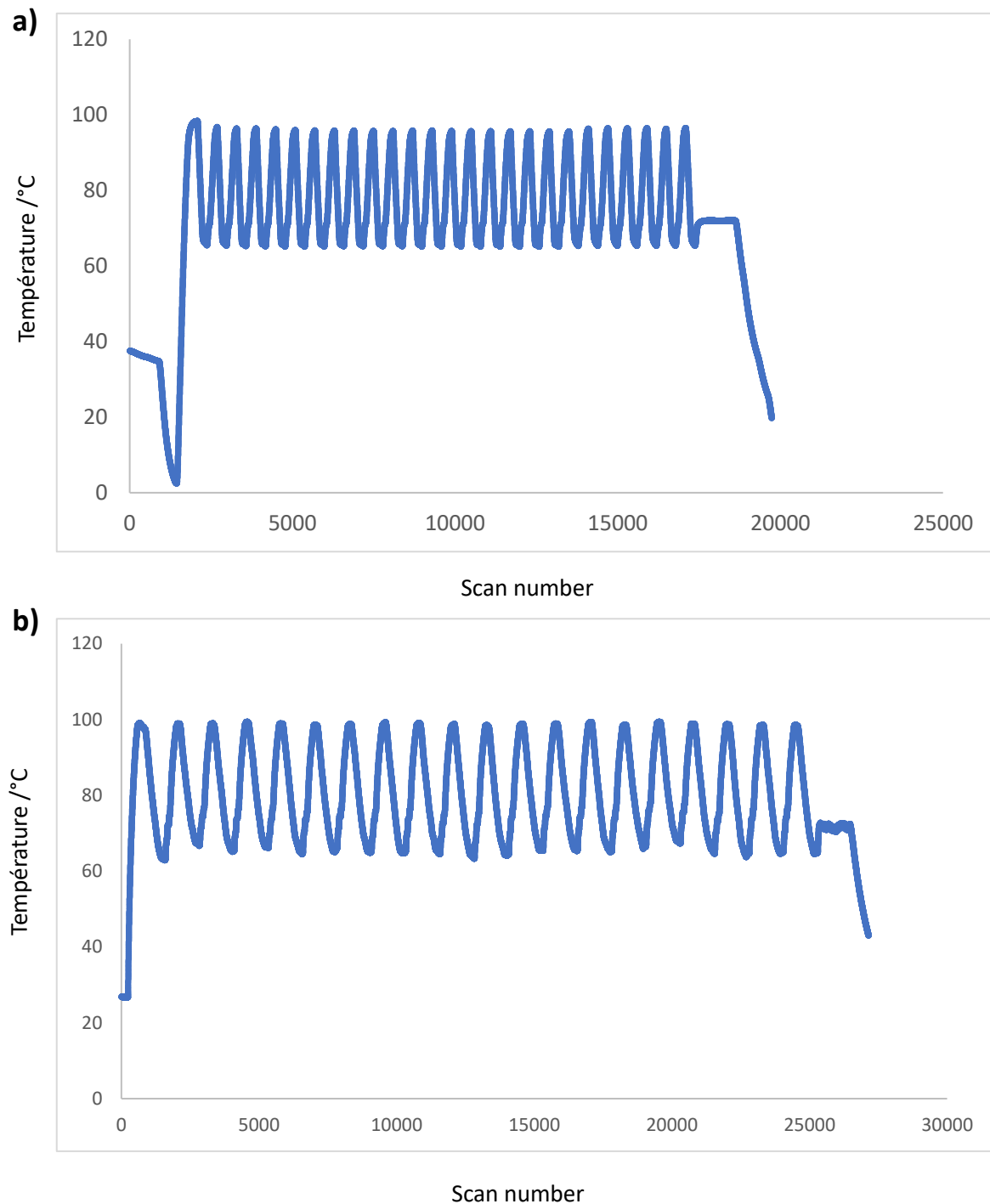


Figure S2. Thermal response of the Bio-Gener (Labgene) thermocycler (a) and the PCRobot (b), as a function of the scan number. Thermal cycling consisted of an initial denaturation at 98 °C for approximately 30 s, followed by cycles including brief denaturation (≈ 10 s at 98 °C), annealing (≈ 15 s at 65 °C), and short extension (≈ 5 s at 72 °C), with a final elongation step of ≈ 2 min at 72 °C.

PCRobot architecture and components.

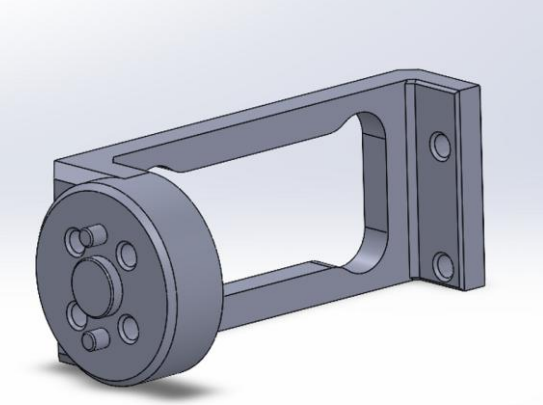
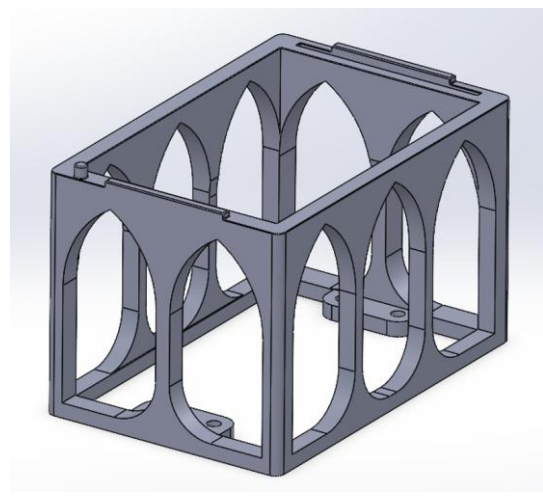
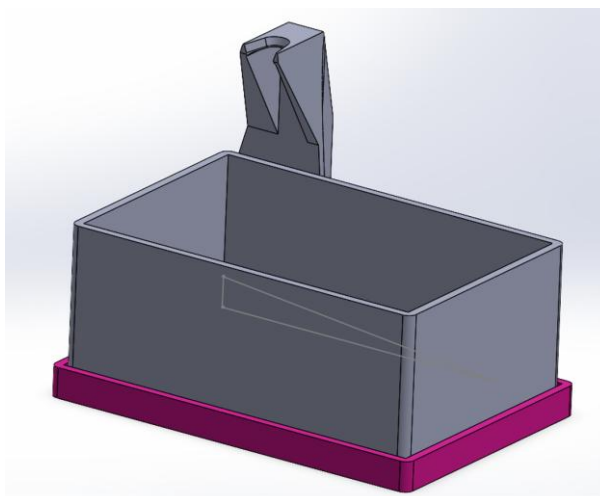
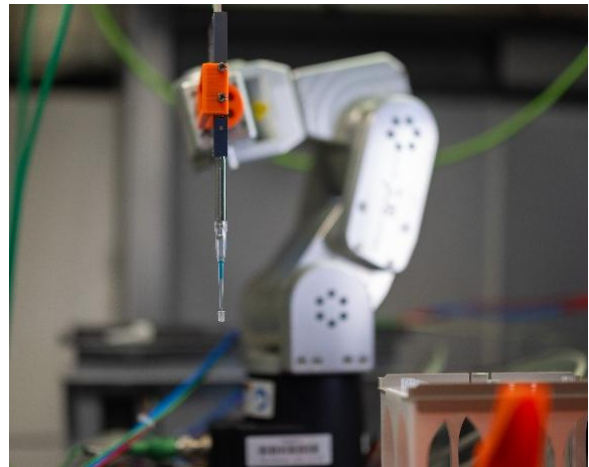
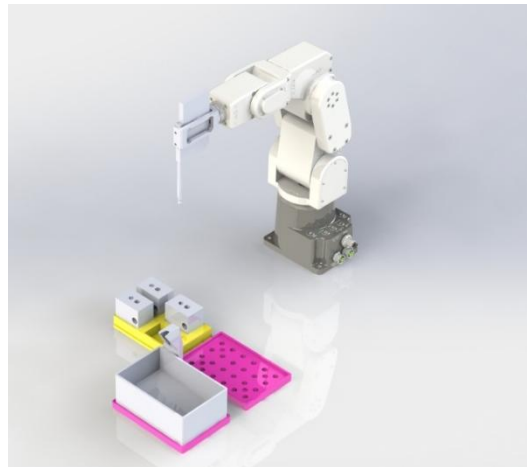


Figure S3. The PCRobot system and components (CAD images and photograph).

Amplification quality comparison.

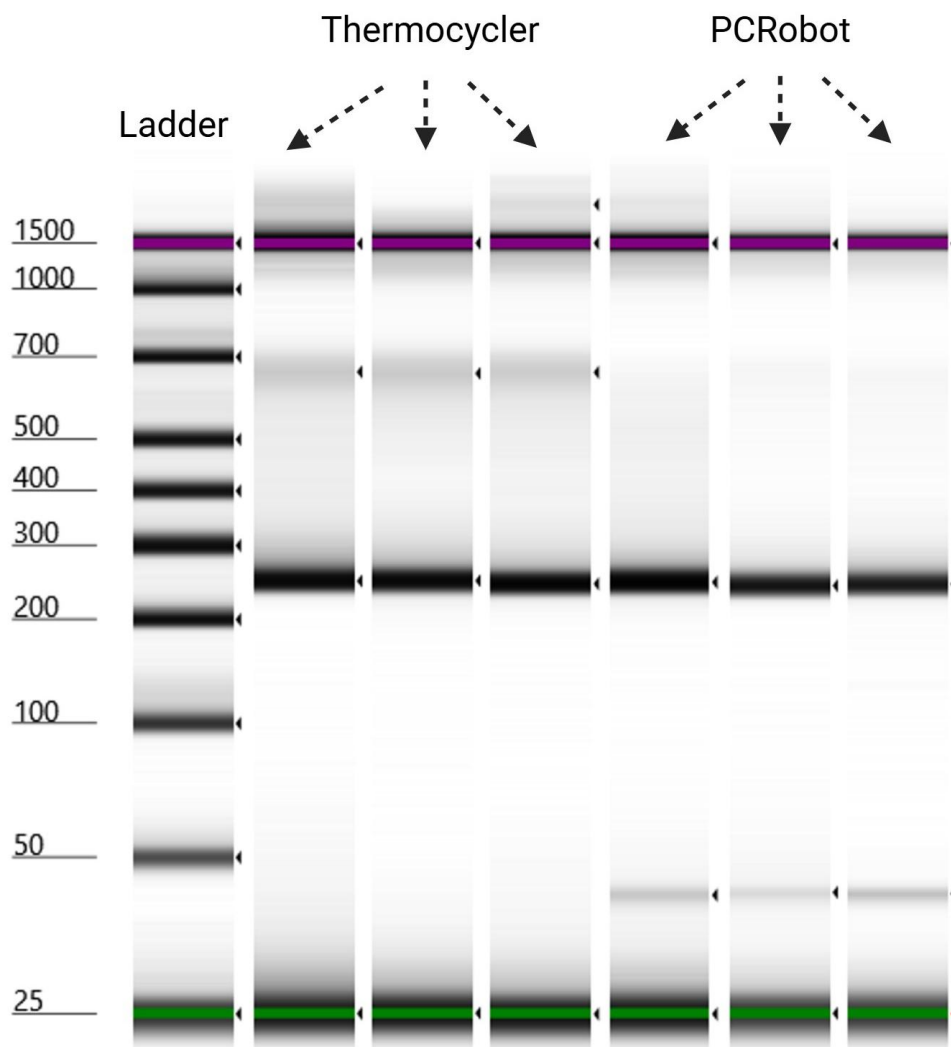


Figure S4. Electropherogram comparing the performance of a Thermocycler with the PCRobot device. Lane 1 - ladder, lanes 2-4 - thermocycler: three replicate samples amplified using a Thermocycler; lanes 5-7 - PCRobot: three replicate samples amplified using the PCRobot device. The band visible across all lanes (2-7) corresponds to the expected PCR product (amplicon). Its location aligns with the 243 bp size marker on the ladder, confirming successful amplification in all six reactions.

Impulse response

The impulse responses of our tips were evaluated using filtered distilled water (20 μL). **Figure S6a)** and **b)** show heating and cooling respectively. Considering the response of 1st order system, $T(t) = T_1 + (T_0 - T_1)(e^{-t/\tau})$, the time constant is measured and the theoretical model of the impulse response can be solved. Resulting time constants for 4 scenarios are shown in Table **S1**.

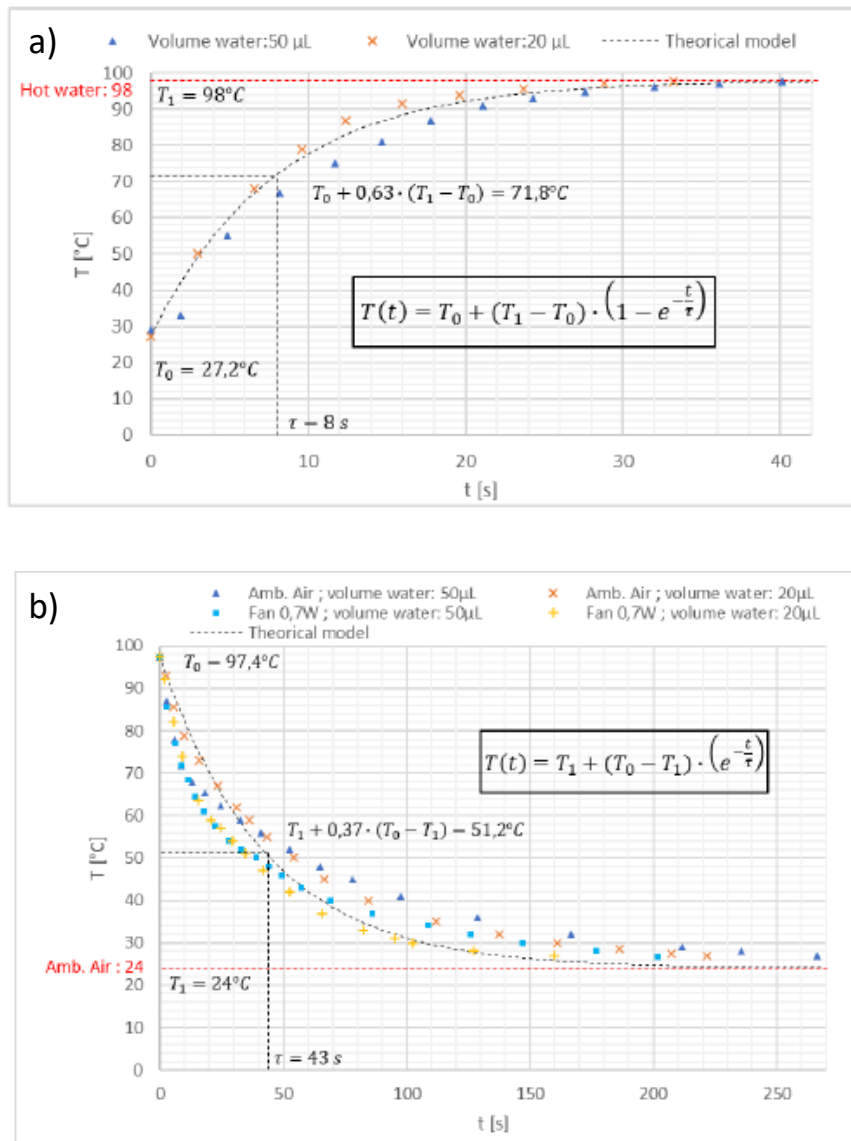


Figure S5. Measure of time constant of the impulse response at a unit step of (a) 98°C (boiling water) and (b) 24°C (ambient air)

Table. S1

Impulse response of 20 μL dH ₂ O in 200 μL tip:		τ [s]
[a]	immersed in water at 98°C (heating).	8
[b]	immersed in water at 76°C (heating).	6,2
[c]	immersed in air at 24°C (cooling).	43
[d]	immersed in water at 54°C (cooling).	6

Caps and mandrel



Figure S6. Custom-made thermocouple and mandrel (photograph and CAD file)

Thermal expansion

When matter changes temperature, it changes shape, area, volume, and density in response. This tendency is called thermal expansion. The polypropylene tip containing the two air columns that trap the PCR solution represented by water will expand. The upper end of the tip is closed by the valve and the lower end is open, Figure.

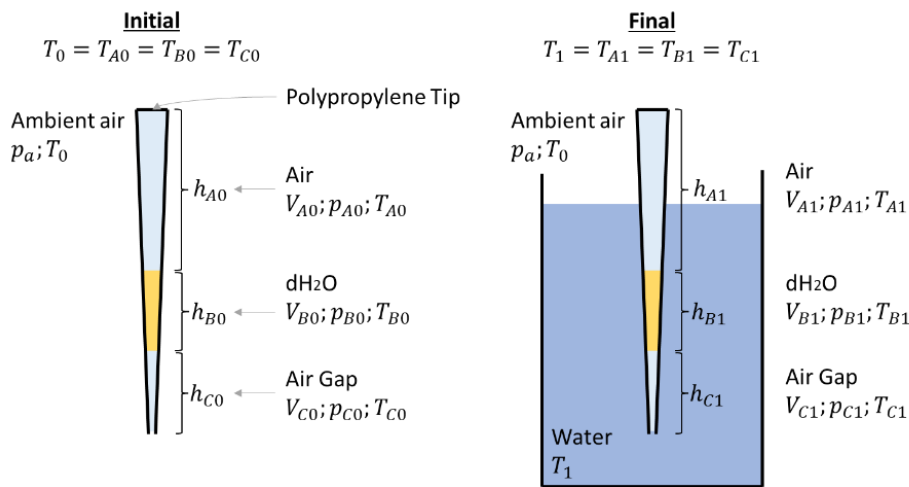


Figure S7. Schematics of thermal expansion of system

In the general case of a gas, liquid, or solid, the volumetric coefficient of thermal expansion is given by:

$$\alpha = \alpha_V = \frac{1}{V} \left(\frac{\partial V}{\partial T} \right)_p \quad [1]$$

The subscript p indicates constant pressure. For linear dimensions we can rewrite:

$$V_{final} = V_{initial} \left(1 + \alpha_V (T_{final} - T_{initial}) \right) \quad [2]$$

Using a linear expansion coefficient for air from Granta EduPack level3: $\alpha_{L\ air} = 3330\ \mu\frac{1}{^{\circ}C}$, the volume of expanded air is calculate to $\Delta V_A = 162\mu L$ and $\Delta V_A = 174\mu L$ for 50 μL and 175 μL tips respectively. These values should not in theory result in any liquid being ejected from the tip, based on experimental air gaps measurements. Therefore, thermal expansion alone cannot explain the liquid loss.

Caps and fabrication

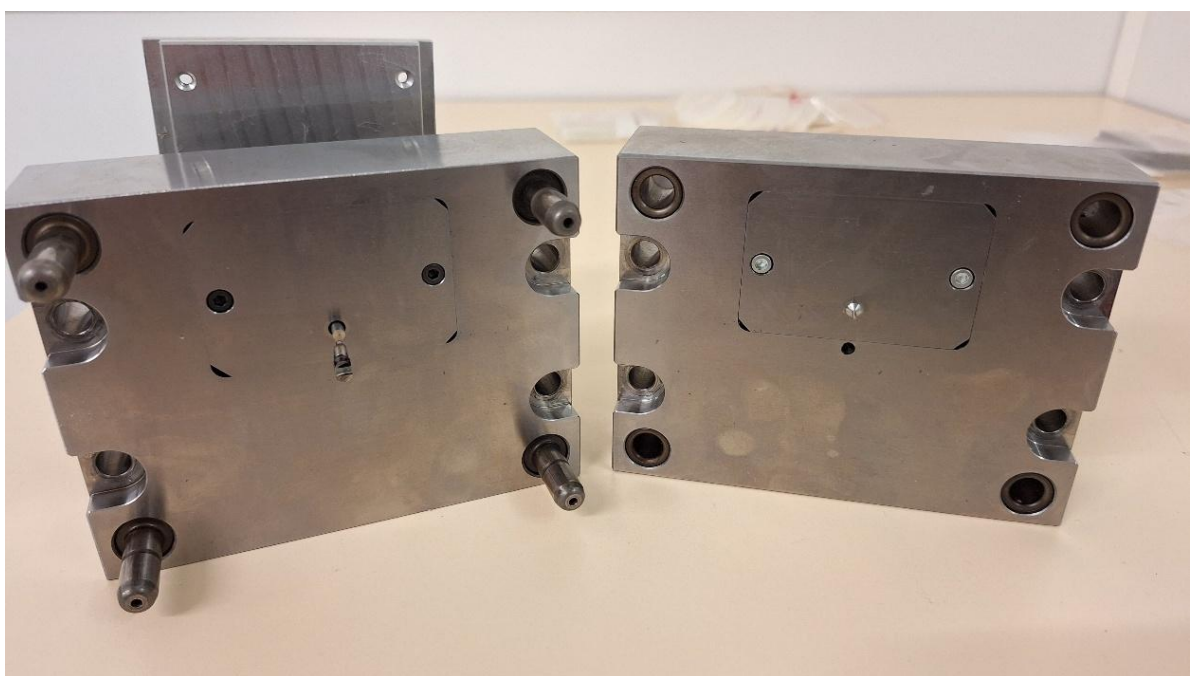
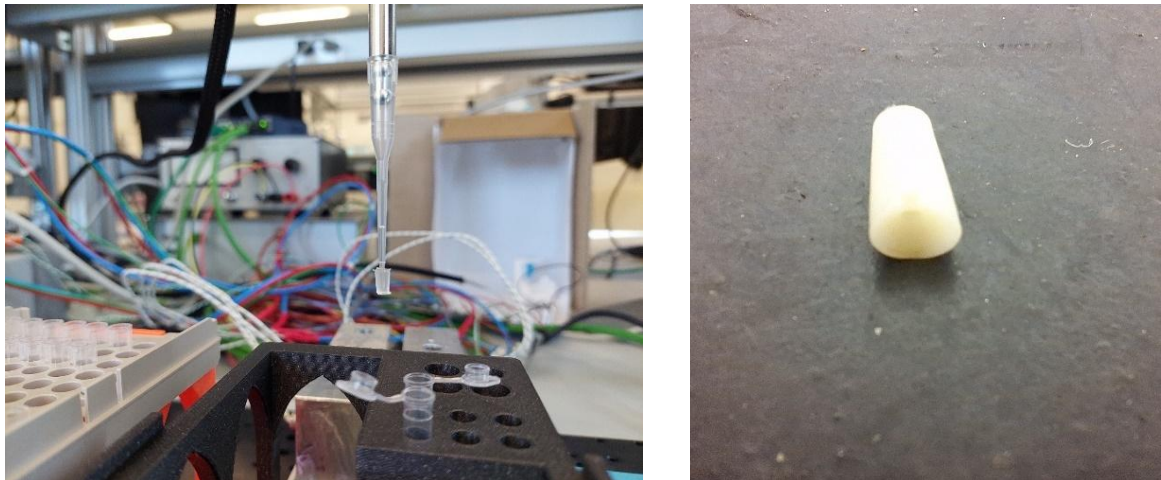


Figure S8. Tips caps and fabrication. using injection moulding. Photographs of the cap on a tip (a), detail of the cap (b) and injection-moulding inserts and bolster moulds (c).

Encoding

DNAMIC logo in svg format was packed into OLOS package and encoded with 30% error correction redundancy. Package size is 8.1KB leading to 352 oligos inside the encoded design file.

CODEC Description.

A DNA-encoded binary file is represented by a list of DNA sequences, called oligonucleotides, with A,T,G, and C sequences of 243 letters on each line making up a text file. Each sequence contains forward and reverse primers of 18 nucleotides (nts) length used for PCR amplification and, in-between, 207 nts for data (Figure 1AS9A). The file identity is mapped to specific forward and reverse primers, randomly generated by sampling a hash function (SHA256) and selected on the basis of Gibbs free energy to optimize PCR, and minimal free energy to avoid secondary structures, and separated by a Hamming distance greater than 10 to limit hybridization between primers. Furthermore, to ensure efficient binding of both primers and avoid asymmetric amplification, the difference between the melting temperatures of the forward and reverse primers must be kept below 2 degrees Celcius.

The data contains error correction codes (inner code), a portion of the file (payload), and an index to identify which part of the file has been encoded. Encoding and decoding are carried out using symbols. A symbol is equivalent to 16 bits encoded by 9 nucleotides (Figure S9B). Input files are treated as byte sequences, transformed into an n by m matrix, where n (number of rows), which corresponds to the payload, is equal to 34 (equivalent to 153 nts), and m (number of columns) is equal to the rounded result of dividing the length of the file byte sequence by 34, to ensure that all data fits into the matrix. If the last column is not filled, it is completed with dummy data, and if the number of columns is odd, an extra column is added with dummy data. To avoid repeating patterns, dummy data are defined by incrementing a counter modulo 256. The index is coded on 4 bytes, making it possible to encode up to a 146 GB file.

Reed–Solomon codes are applied to detect and correct multiple symbol errors for matrix columns (inner codes) and matrix rows (outer codes). The inner code, represented by 8 bytes, is added to the first row of the matrix (see Figure 1CS9C). The outer code is calculated for each row joining two bytes (which is why an extra column is added if the number is odd). Since an RS symbol is equivalent to 16 bits, the maximum number of bytes that can be used to represent columns is 131070 bytes. Beyond this size, the matrix must be separated into blocks.

Considering the target redundancy r , which depends on the error rate resulting from the various DNA processes (i.e. synthesis, preservation, PCR, and sequencing), the number e_c corresponding to the outer code columns added to each block is given by

$$e_c = \frac{r \cdot \min(m, 131070)}{1 - r}$$

with e_c rounded to even. On the basis of sequencing experiments using nanopore technology, we set r in the 10-30% range. The minimum (rounded up) of n_b blocks required to store all information (excluding the outer code) is therefore

$$n_b = \frac{m}{131070 - e_c}$$

Blocks can contain different amounts of data, and, to distribute symbols evenly, the average number of bytes required per block is

$$\bar{m} = \frac{m}{n_b}$$

with \bar{m} rounded to even.

The 2-byte conversion is achieved by mapping three Galois Field (GF) elements of size 41 by base conversion (256^2 to 41^3). Individual columns are converted to DNA using the GF(41) codon wheel shown in Figure 1B, ensuring that no base is repeated more than three times.

Primer sequences used for amplification are ACGAGCGTGAGTACTCTG for forward primer and CGCCAGCTCCAGTCGGTG for reverse primer.

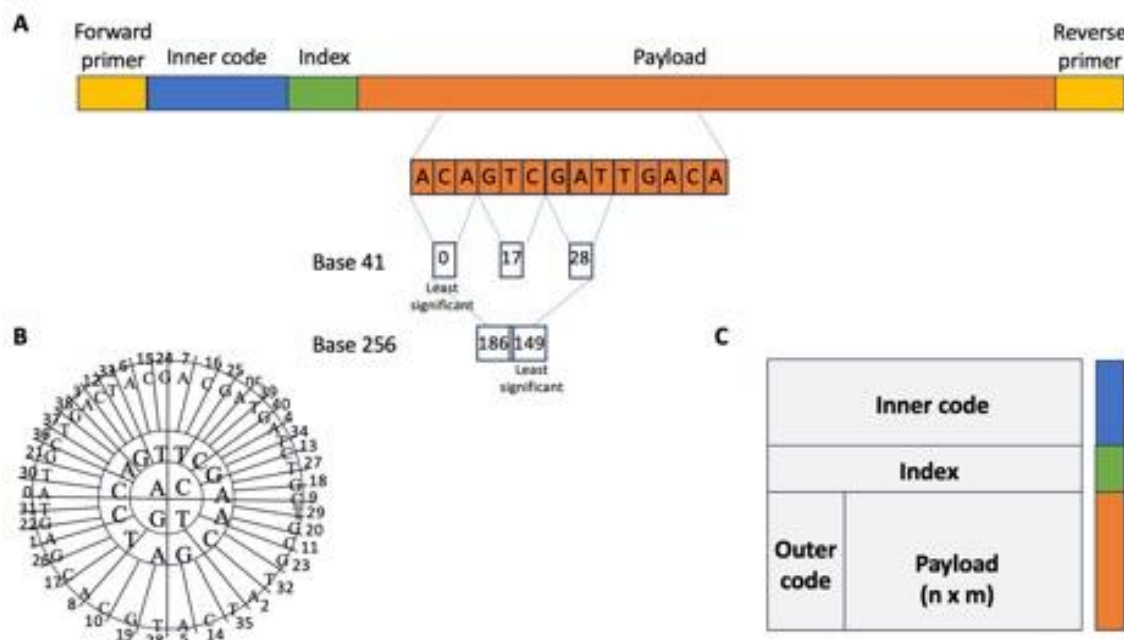


Figure S9. A) Details of the oligonucleotide structure, with an illustration of a 2-byte-to-nucleotides conversion; B) GF(41) is derived from the codon wheel; C) General block structure.